Interannual-decadal variability of wintertime mixed layer depths in the North Pacific detected by an ensemble of ocean syntheses

Article

Accepted Version

Publisher: Springer

www.reading.ac.uk/centaur

CentAUR

Central Archive at the University of Reading

Reading's research outputs online

1 **Title**

2 Interannual-decadal variability of wintertime mixed layer depths in the North Pacific detected by

3 an ensemble of ocean syntheses.

4

5 **Authors**

6 Takahiro Toyoda, Yosuke Fujii, Tsurane Kuragano, Naohiro Kosugi, Daisuke Sasano, and

7 Masafumi Kamachi (Meteorological Research Institute, Japan Meteorological Agency

8 (MRI/JMA), Tsukuba, Japan)

9 Yoichi Ishikawa (Center for Earth Information Science and Technology, Japan Agency for

10 Marine-Earth Science and Technology (CEIST/JAMSTEC), Yokohama, Japan)

11 Shuhei Masuda, and Kanako Sato (Research and Development Center for Global Change

12 (RCGC), JAMSTEC, Yokohama, Japan)

13 Toshiyuki Awaji (CEIST/JAMSTEC, Yokohama, Japan; Kyoto University, Kyoto, Japan)

14 Fabrice Hernandez (Institut de Recherche pour le Développement (IRD), Toulouse, France;

15 Mercator Océan, Ramonville Sant-Agne, France)

16 Nicolas Ferry (Mercator Océan, Ramonville Sant-Agne, France)

17 Stéphanie Guinehut (Collecte Localisation Satellites (CLS), Ramonville Sant-Agne, France)

18 Matthew Martin, K. Andrew Peterson, and Simon A. Good (Met Office, Exeter, UK)

19 Maria Valdivieso, and Keith Haines (National Centre for Earth Observation (NCEO),

20 Department of Meteorology, University of Reading (U-Reading), Reading, UK)

21 Andrea Storto (Centro Euro-Mediterraneo sui Cambiamenti Climatici (CMCC), Bologna, Italy)

22 Simona Masina (CMCC; Istituto Nazionale di Geofisica e Vulcanologia (INGV), Bologna,

23 Italy)

24 Armin Köhl (Universität Hamburg (U-Hamburg), Hamburg, Germany)

25 Yonghong Yin, Li Shi, and Oscar Alves (Centre for Australian Weather and Climate Research,

26 Bureau of Meteorology (BOM), Melbourne, Australia)

27 Gregory Smith (Environment Canada, Québec, Canada)

28 You-Soon Chang (Geophysical Fluid Dynamics Laboratory, National Oceanic and Atmospheric

29 Administration (GFDL/NOAA), Princeton, New Jersey, USA; Kongju National University,

30 Kongju, South Korea)

31 Guillaume Vernieres (Science System and Applications, Inc., Lanham, Maryland, USA; Global

32 Modeling and Assimilation Office, National Aeronautics and Space Administration Goddard

33 Space Flight Center (GSFC/NASA/GMAO), Greenbelt, Maryland, USA)

34 Xiaochun Wang (Joint Institute for Regional Earth System Science and Engineering, University

35 of California, Los Angeles, California, USA)

36 Gael Forget, and Patrick Heimbach (Department of Earth, Atmospheric and Planetary Sciences,

37 Massachusetts Institute of Technology (MIT), Cambridge, Massachusetts, USA)

38 Ou Wang, Ichiro Fukumori, and Tong Lee (Jet Propulsion Laboratory (JPL), California Institute

39 of Technology, Pasadena, California, USA)

40 Hao Zuo, and Magdalena Balmaseda (European Centre for Medium-Range Weather Forecasts

41 (ECMWF), Reading, UK)

42

43 **Corresponding author**

44 Takahiro Toyoda, Oceanography and Geochemistry Research Department, Meteorological

45 Research Institute, Japan Meteorological Agency, 1-1 Nagamine, Tsukuba, 305-0052, Japan

46 E-mail: ttoyoda@mri-jma.go.jp

47

48

49   **Abstract**

50

51   The interannual-decadal variability of the wintertime mixed layer depths (MLDs) over the North

52   Pacific is investigated from an empirical orthogonal function (EOF) analysis of an ensemble of

53   global ocean reanalyses. The first leading EOF mode represents the interannual MLD anomalies

54   centered in the eastern part of the central mode water formation region in phase opposition with

55   those in the eastern subtropics and the central Alaskan Gyre. This first EOF mode is highly

56   correlated with the Pacific decadal oscillation index on both the interannual and decadal time

57   scales. The second leading EOF mode represents the MLD variability in the subtropical mode

58   water (STMW) formation region and has a good correlation with the wintertime West Pacific

59   (WP) index with time lag of 3 years, suggesting the importance of the oceanic dynamical

60   response to the change in the surface wind field associated with the meridional shifts of the

61   Aleutian Low. The above MLD variabilities are in basic agreement with previous observational

62   and modeling findings. Moreover the reanalysis ensemble provides uncertainty estimates. The

63   interannual MLD anomalies in the first and second EOF modes are consistently represented by

64   the individual reanalyses and the amplitudes of the variabilities generally exceed the ensemble

65   spread of the reanalyses. Besides, the resulting MLD variability indices, spanning the 1948-

66   2012 period, should be helpful for characterizing the North Pacific climate variability. In

67   particular, a 6-year oscillation including the WP teleconnection pattern in the atmosphere and

68   the oceanic MLD variability in the STMW formation region is first detected.

69

70

71   **Keywords**

72 ocean reanalysis, mixed layer depth, North Pacific, mode water, Pacific decadal oscillation,

73 West Pacific teleconnection pattern

74

75

76 **1 Introduction**

77

78 Most of the properties of the water masses in the global ocean are determined by the air-sea

79 interaction and turbulent mixing within the surface mixed layer (ML) and by subduction down to

80 the ventilated thermocline layer (Pedlosky 1996). The ML processes, hence, characterize the heat

81 and freshwater cycle in the upper ocean and are also an important component of the bio-

82 geochemical cycle (e.g., Takahashi 1997). Since the amount of subduction from the ML is largely

83 dependent upon the spatial distribution of the mixed layer depth (MLD) (e.g., via lateral induction;

84 Huang and Qiu 1994), the water-mass variability is strongly affected by the spatio-temporal MLD

85 variability. Accurate description of the latter is therefore required for better understanding and

86 characterizing the climate variability.

87

88 Previous studies have described the observed features of global MLD distribution based on the

89 climatological temperature and salinity (TS) data (e.g., Levitus 1982; Monterey and Levitus 1997;

90 Kara et al. 2003). de Boyer Montegut (2004) estimated the monthly variation in the global MLD

91 distribution by processing individual profiles of the TS observations. These studies have clarified

92 global features in the seasonal cycle of MLD climatology. Recently, observations by the Argo

93 hydrographic array have facilitated the description of the interannually-varying global MLD

94 distribution (e.g., Hosoda et al. 2010). However, the spatial resolution and temporal coverage of

95 the Argo data are still limited, particularly since decent coverage is practically limited to the last

96   century, which restricts applications to time scales of less than a decade.

97

98   The interannual-decadal variability of the MLDs in the water-mass formation regions has been

99   investigated in association with the analysis of water masses, such as mode waters (e.g., Hanawa

100   and Talley 2001; Speer and Forget 2013), by both observational and modeling studies (e.g., Peng

101   et al. 2006; Joyce et al. 2009). In the North Pacific, the most prominent interannual-decadal

102   variability is known to be the Pacific decadal oscillation (PDO; Kawasaki 1991), which is often

103   characterized by the "PDO index" as defined by the leading principal component of the North

104   Pacific sea surface temperature (SST) variability poleward of 20°N (Mantua et al. 1997). A

105   stronger (weaker) Aleutian Low along with stronger (weaker) westerlies and lower (higher) SSTs

106   in the western-central North Pacific is represented by a positive (negative) PDO index. Several

107   studies have explored the MLD variation in the formation region of the central mode water

108   (CMW; ~$26.2\sigma_{\theta}$, 9-12ºC; Suga et al. 1997) in response to the PDO, particularly the decadal (or

109   interdecadal) regime shifts associated with the PDO (such as in 1976-1977) (e.g., Deser et al.

110   1996; Yasuda and Hanawa 1997; Schneider et al. 1999; Yasuda et al. 2000; Ladd and Thompson

111   2002; Qu and Chen 2009).

112

113   In addition to the aforementioned MLD variability in the CMW formation region, recent studies

114   (e.g., Qiu and Chen 2006; Qiu et al. 2007; Oka 2009) have investigated another important MLD

115   variability in the Kuroshio recirculation gyre region, where the subtropical mode water (STMW;

116   ~$25.2\sigma_{\theta}$, 15-19ºC; Masuzawa 1969) is formed. They showed that the sea surface height and main

117   thermocline depth anomalies generated by the wind stress curl anomalies in the central subtropics

118   propagate westward and then influence the Kuroshio recirculation gyre region, leading to the

119   changes in the wintertime MLD and STMW thickness with time lag of a few years (e.g., Qiu and

120 Chen 2005). In these studies, the wind stress curl variability in the central subtropics is mainly

121 attributed to the Aleutian Low activity and hence can be related to the PDO index (e.g., Oka and

122 Qiu 2012) or to similar indices related with variations in the intensity of the Aleutian Low (e.g.,

123 North Pacific index (NPI; Trenberth and Hurrell 1994)). On the other hand, Sugimoto and Hanawa

124 (2010) proposed that the meridional shifts of the Aleutian Low are more important in explaining

125 the variability in the Kuroshio recirculation gyre region than the change in intensity of the

126 Aleutian Low represented by the PDO index. Meridional shifts of the Aleutian Low are related to

127 the West Pacific (WP) teleconnection pattern (Wallace and Gutzler 1981) and do not correlate

128 significantly with the intensity variation (Sugimoto and Hanawa 2009). Therefore, conflicting

129 causes have been suggested for the MLD variability in the Kuroshio recirculation gyre region

130 based on relatively short-term observation analyses: one group pointed out the dominant role of

131 the change in intensity of the Aleutian Low, and another group suggested the influence of the

132 meridional movement of the Aleutian Low. These should be investigated based on reliable long-

133 term products.

134

135 Subject to the El Niño-Southern Oscillation, the PDO pattern exhibits the interannual modulation

136 (e.g., Newman et al. 2003). The accurate description of the interannual-decadal MLD variability

137 on the basin scale is thus required for further understanding and characterizing the water-mass

138 variability in relation to the climate variability in the North Pacific (e.g., PDO). Although the

139 interannual variability of the MLDs on the basin scale has recently been investigated using the

140 Argo float data (e.g., Oka et al. 2007), this is arguably a very short period. Therefore, it is of value

141 to identify the long-term basin-scale MLD variability by fully utilizing observational datasets

142 available and our knowledge of the ocean dynamics (e.g., ocean models).

143

144 Ocean syntheses use the output of dynamical models combined with observations using statistical

145 technique and hence can provide MLDs at every defined grid point and time step, although they

146 are inevitably influenced by errors in the dynamical models, observations and assimilation

147 methods. Due to the recent increase in a variety of observations and in response to advances in

148 modeling and assimilation techniques, ocean syntheses have been improved to the level for

149 practical use (e.g., Lee et al. 2009). For example, Toyoda et al. (2011) analyzed the relative

150 contributions of the 3 dominant physical processes to the interannual variability of the North

151 Pacific eastern subtropical mode water (ESTMW; 24.0-25.4σ_θ, 16-22°C; Hautala and Roemmich

152 1998) formation due to the wintertime ML deepening, by using an ocean state estimation product

153 obtained by a 4 dimensional variational data assimilation experiment for the 1990s. This analysis

154 should be revisited for the more recent period using the Argo float data, especially since the

155 salinity observations are needed for the reproduction of the ML properties (Oka and Qiu 2012).

156 In addition, new ocean synthesis products have continuously been generated by different

157 institutions. Therefore, it is appropriate to revise the MLD estimates using the last generation of

158 ocean synthesis products.

159

160 To promote the increased use of ocean syntheses, the Global Synthesis and Observations Panel

161 (GSOP) of the Climate Variability and Predictability (CLIVAR) has recently initiated the Ocean

162 Reanalyses Intercomparison Project (ORA-IP), whose major goal is the inter-evaluation of global

163 ocean syntheses produced in the operational and research centers from various aspects (MLD,

164 heat and salt content, steric height, sea level, surface heat fluxes, depth of the 20 degree isotherm

165 and sea ice; Balmaseda et al. 2015). As part of this project work, Toyoda et al. (2015) have

166 investigated the fidelity in MLD of a suit of global ocean estimates consisting of two model-

167 independent estimates, produced by using only observations and 17 ocean syntheses, produced

168   using data assimilation approaches that combine ocean models and observations based on the

169   maximum likelihood principle ("reanalyses" hereafter). In addition to the discussion on biases in

170   the MLDs of the individual syntheses, they demonstrated that the skillful MLD reproduction for

171   both the seasonal cycle and interannual variability is possible by using the ensemble mean of the

172   reanalyses. They discussed that ocean reanalyses effectively synthesize oceanic and atmospheric

173   (via surface forcing from atmospheric reanalyses) observations and the dynamical models, with

174   their model errors cancelling out through ensemble averaging, suggesting great potential for better

175   analyzing the upper ocean processes.

176

177   In this study, we focus on the interannual-decadal variability of the wintertime MLDs in the North

178   Pacific represented in the ensemble mean of the reanalyses. The ensemble mean MLD field along

179   with information on its uncertainty derived from the ensemble spread allows a more quantitative

180   investigation than previous analyses (e.g., Toyoda et al. 2011). The aforementioned study (Toyoda

181   et al. 2015) focused on the validation of MLDs from ocean reanalyses using the Argo float data

182   (e.g., Hosoda et al. 2010). The current study, however, is not limited to the Argo era, but covers

183   the full temporal record of the reanalyses, which allows analyzing the relationship between the

184   MLD variability in the North Pacific and the interannual-decadal scale climate variability. Section

185   2 describes the ensemble mean MLD field derived from the reanalyses as well as other datasets

186   used in this study. The North Pacific MLD variability on an interannual-decadal time scale is

187   investigated in section 3. The summary and discussion are given in section 4.

188

189

190   **2 Data**

191

192   Monthly MLD fields estimated from 2 observation-only analyses and 17 reanalyses (Table 1) are

193   provided by the operational and research centers as an ORA-IP activity. These

194   syntheses/reanalyses are all different in ocean general circulation model, resolution, surface

195   forcing, ML parameterization, assimilated data and assimilation method (see details in Toyoda et

196   al. 2015). MLDs are obtained from the monthly mean TS fields on the original grids for the

197   individual datasets and then interpolated onto the common longitude-latitude grids at one-degree

198   intervals.

199

200   In the present study, we use a density criterion for the MLD definition (e.g., Levitus 1982), i.e.,

201   MLD is defined as the depth where potential density exceeds the 10-m depth value by 0.125 kg

202   m^{-3}. Toyoda et al. (2015) revealed that this definition results in an MLD field with less errors

203   relative to definitions using other criteria for potential density (0.03 kg m^{-3}) or potential

204   temperature (0.2°C and 0.5°C) in terms of both the seasonal cycle and interannual variability

205   since errors due to monthly averaging of profiles and to weak thermal stratification at high

206   latitudes are relatively small with this definition. Moreover, we use only wintertime maximum

207   MLDs, since we consider that such MLDs are thought to be a most important factor for the

208   thermocline layer dynamics via water mass formation and subduction. Note that the interannual

209   variability in MLD is generally dominated by the interannual variability of the wintertime MLDs

210   (except for the tropics). We pick out a wintertime maximum MLD in each location, year and

211   dataset from January-April (July-October) in the Northern (Southern) Hemisphere. These months

212   are chosen on the basis of the histogram for occurrence of the annual maxima of all the synthesis

213   MLDs (Fig. 1a). Although months when maximum MLDs occur can differ in each location within

214   the North Pacific (Fig. 1b), our approach allows the integrated analysis of the important MLD

215   features in the whole basin. Climatologies are defined for the wintertime maximum MLDs during

216   the 2001-2011 period (or longest available during this period). Hence, the month for producing

217   the climatology can vary among years at each grid point. Interannual anomalies from their

218   respective climatology are calculated for the individual products. Ensemble mean of the

219   climatology and interannual anomalies are then obtained from this ensemble of climatologies and

220   interannual anomalies (not including the observation-only analyses). Ensemble mean time series

221   (for the 1948-2012 period) are constructed by using these climatology and interannual anomaly

222   fields (referred to as "ENSMEAN" hereafter). Therefore, the number of reanalysis products

223   entering the ensemble mean time series varies with time, since the reanalyses products span

224   different time periods.

225

226   Monthly time series of the PDO index for the 1900-2014 period are obtained from the website of

227   the Joint Institute for the Study of the Atmosphere and Ocean, University of Washington

228   (http://jisao.washington.edu/pdo/PDO.latest). We calculate the year-to-year wintertime PDO time

229   series by averaging the monthly data from December of the preceding year to February of the

230   target year. We also use the annual PDO time series defined as the average from July of the

231   preceding year to June of the target year (with its center in winter) in order to compare with the

232   above wintertime time series.

233

234   Monthly time series of the WP index are obtained from the website of the National Weather

235   Service Climate Prediction Center, National Ocean Atmosphere Administration

236   (http://www.cpc.ncep.noaa.gov/data/teledoc/wp.shtml). Wintertime and annual WP time series

237   are calculated in the same manner as the PDO time series.

238

239   In addition, we use the JMA's historical observational data along the 137°E line in the North

240   Pacific in order to evaluate our results. Time series of temperatures in the STMW core in summer

241   at 137 $^{\text{o}}$ E are obtained from the JMA website

242   (http://www.data.jma.go.jp/gmd/kaiyou/data/shindan/b_1/stmw/npstmw137e.txt). Observation

243   data of the geochemical parameters (nitrate concentration and apparent oxygen utilization (AOU))

244   are also obtained from the JMA website

245   (http://www.data.jma.go.jp/gmd/kaiyou/db/vessel_obs/data-report/html/ship/ship.php) and

246   interpolated onto the $25.2\sigma_\theta$ density surface through the Akima (1970) method after quality

247   control in the MRI. Annual mean values are calculated from the monthly time series averaged

248   over 28^oN-32^oN.

249

250   We use the monthly values for sea level pressure (SLP) and latent and sensible heat fluxes from

251   both the JRA-55 (Kobayashi et al. 2015) and CORE (Large and Yeager 2004) datasets. The

252   COBE-SST (Ishii et al. 2005) dataset is also used.

253

254

255   **3. Result and discussion**

256

257   **3.1. Features of the ensemble mean field**

258

259   In this section, we explore the variability of the wintertime maximum MLDs in the North Pacific,

260   by taking advantage of the ensemble mean of the reanalysis MLDs (ENSMEAN). In doing so, we

261   first investigate the fidelity of ENSMEAN using metrics for evaluating our ensemble approach,

262   which are based on the ensemble spread and the correlation analysis.

263

264   Figure 2 shows the spatial distributions of the reanalysis ensemble mean and spread of the

265   wintertime maximum MLDs for the 2001-2011 period. Ensemble spread is defined here as the

266   standard deviation of the departure of each reanalysis from the ensemble mean at each grid point

267   and each year (e.g., Xue et al. 2012), which gives a measure of the uncertainty in the ensemble

268   mean. The ensemble spread distribution for the absolute wintertime maximum MLDs (Fig. 2b)

269   shows relatively large values in regions of large ensemble mean MLDs (Fig. 2a) such as in the

270   subarctic North Atlantic. A similar relation can be seen between the ensemble spread (Fig. 2d)

271   and the standard deviation of the ensemble mean (Fig. 2c) for the interannual anomalies (see

272   definition in Section 2). In addition, large values for the ensemble spread can be seen in the polar

273   regions, where large estimation errors of MLD were reported to arise primarily from the poor

274   potential of both model and assimilation experiments in representing the physical processes there

275   (e.g., deep convection and sea ice processes; see Toyoda et al. 2015). In the North Pacific, the

276   ensemble spread values for the absolute MLDs are mostly smaller than 60 m in the Kuroshio

277   Extension region and the Bering and Okhotsk Seas, where the ensemble mean MLDs are larger

278   than 150 m. On the other hand, the ensemble spread values are generally smaller than 20 m in

279   other regions of smaller MLDs. Note that the large values located in the northern part of the Japan

280   Sea are caused by the differences in both the amplitude and location between the reanalyses in

281   associattion with the small-scale deep convections off the Vladivostok (e.g., Senjyu and Sudo

282   1994). For the interannual anomalies, the ensemble spread values are even smaller: 30-40 m in

283   the Kuroshio Extension region and less than 10 m in most of the other open seas (Fig. 2d). These

284   values, in particular for the interannual anomalies, will be compared with the amplitude of the

285   analyzed variability in the following subsections. Note that, since the signal (standard deviation

286   of the ensemble mean anomalies) to noise (spread around the ensemble mean anomalies) ratio is

287   generally near 1 (Fig. 2e), the signal may not be well resolved.

288

289   The ensemble spread provides important information on the uncertainty of the ensemble mean

290   field based on root mean square differences. However, it gives no information about whether

291   ensemble members are exhibiting the same variability, i.e., the sign of the anomaly cannot be

292   properly evaluated by this metric. This is particularly in the present case that the amplitudes of

293   the variations in the individual reanalyses may differ depending on their configurations (e.g.,

294   mixed layer models). A better indicator of coordinated behavior would be the correlation between

295   the ensemble members and ensemble mean. In this study, we will use the averaged correlation of

296   all ensemble members with the ensemble mean as a qualitative indicator of a coordinated response

297   among the ensemble members.

298

299   Figure 3 exhibits the averaged correlation coefficients for the interannual anomalies between

300   ENSMEAN and the individual reanalyses. These values indicate the degree of consistency in

301   representing the interannual anomalies by the individual products. Hence, in addition to the

302   ensemble spread, the above values can be used for assessing the fidelity of the interannual

303   anomaly field of ENSMEAN. In this study, we underline the consistency in the signs of the

304   interannual anomalies. Therefore, we use the ENSMEAN MLDs only in those regions where the

305   averaged correlation coefficients between ENSMEAN and the individual reanalyses exceed the

306   90% confidence level (0.521). Although the regions with relatively large ensemble spread values

307   (e.g., in the Bering, Okhotsk and Japan Seas) are mostly eliminated by this procedure, we further

308   direct our attention to the open ocean region of the North Pacific (as indicated by the purple line

309   in Fig. 3) in the following analysis, in order to eliminate grid-scale un-eliminated data in the

310   marginal seas (the Okhotsk, Japan and East China Seas).

311

312 Before the analysis of the wintertime maximum MLDs of ENSMEAN, we compare those between

313 ENSMEAN and the observation-only analyses (EN3v2a and ARMOR3D). Figure 4 shows the

314 correlation coefficients among the 3 datasets. The correlations between EN3v2a/ARMOR3D and

315 ENSMEAN are generally greater than the correlation between the observation-only products in

316 most of the open ocean region. The comparison of the zonal mean values implies that this feature

317 is pronounced at low- and mid-latitudes (Fig. 4d). This is in contrast to the averaged correlation

318 between the observation-only analyses and the individual reanalyses (dashed lines) which is lower

319 than the correlation between the observation-only analyses. These results for the wintertime

320 maximum MLDs are similar to the previous results for the whole monthly MLDs (Toyoda et al.

321 2015) and suggest a skillful reproduction of the interannual anomaly field for the wintertime

322 maximum MLDs thanks to the ensemble averaging approach using the reanalysis estimates.

323

324 **3.2 Variability in the central subtropical North Pacific**

325

326 We perform an empirical orthogonal function (EOF) analysis for the interannual anomalies of the

327 wintertime maximum MLDs of ENSMEAN in the open ocean region of the North Pacific (within

328 the region bounded by the purple line in Fig. 3), and with the consistency of the ensemble

329 members at the 90% confidence level (correlation coefficients above 0.521 – the orange/red

330 regions in Fig. 3; thus, the Bering Sea is partly included, but only the small portions that exceed

331 the required consistency level) for the 2001-2011 period. This period is chosen because it is

332 common to most of the reanalyses (Table 1) and the Argo data are available for assimilation

333 throughout, although the full deployment of the Argo array was achieved by around 2004. Figure

334 5 shows the patterns and intensities of the first and second leading EOF modes for the 2001-2011

335 period ("EOF-1" and "EOF-2" hereafter), which explain 41% and 20% of the interannual

336 anomalies, respectively. Higher modes exhibit variations on much smaller scales and explain the

337 variance of less than 8% and will not be discussed any further in this study. Note that, in Fig. 5b,

338 d, projected time series of the EOF patterns are plotted for the other period of the EOF analysis

339 (before 2000 and for 2012; thin red lines).

340

341 For estimation of the influence of the selected period on the analysis, we perform another EOF

342 analysis for the same ENSMEAN interannual anomalies in the open ocean region of the North

343 Pacific for the whole 1948-2012 period. The first two EOF spatial patterns (Fig. 5a, c) and

344 principal components (PCs; "PC-1" and "PC-2" hereafter) (Fig. 5b, d) are basically similar to

345 those from the EOF analysis for the 1948-2012 period (e.g., red and blue lines for the PCs of the

346 2001-2011 and 1948-2012 EOF analyses, respectively), although the EOF spatial patterns for the

347 2001-2011 period show relatively confined structures with greater peak values (not shown). We

348 also compute the PC time series by projecting anomalies with respect to the 1948-2012 period

349 onto the EOF pattern based on the 2001-2011 period as discussed by Wen et al. (2014). The

350 resulting time series are further similar to the PCs from the EOF analysis for the 2001-2011 period.

351 This lends support to our expectation that the influence of the selected period to our below results

352 is negligible.

353

354 The EOF-1 pattern shows positive values in the western-central North Pacific while negative

355 values in the surrounding region (Fig. 5a). This pattern is similar to the SST distribution of the

356 PDO: negative (positive) SST anomalies of the PDO index correspond to positive (negative) MLD

357 anomalies of the EOF-1, consistent with previous studies (e.g., Ladd and Thompson 2002). Figure

358 6a indicates that the PC-1 (red line) actually correlates quite well with the wintertime PDO time

359 series (blue line), not only during the 2001-2011 period where the correlation coefficient is 0.77,

360   significantly non-zero at the 99% confidence level, but over the past 53 years (1948-2000) where

361   the correlation coefficients is 0.58 representing an even higher confidence level by virtue of the

362   larger temporal sample size. These results indicate that the MLD variability in this region is by

363   and large reproduced by ENSMEAN with a certain quality during the whole data period. Note

364   that the wintertime (December-February) time series are used here since the atmosphere-ocean

365   interaction is strong in this season (e.g., Trenberth and Hurrell 1994).

366

367   In the EOF-1 pattern (Fig. 5a), large positive values up to 30-40 m can be seen in the central

368   subtropics. This region corresponds to the eastern part of the CMW formation region. The typical

369   amplitude of this variability (Fig. 2c) averaged over this region (180°-160°W, 32°N-42°N; purple

370   box in Fig. 5a) is 30 m, while the ensemble spread of the interannual anomalies for ENSMEAN

371   (Fig. 2d) averaged over this region is 26 m. This suggests that the analyzed variability is generally

372   reliable when the amplitudes of the PC-1 are greater than the ratio of these values (0.87; Fig. 2e)

373   approximately. Moreover, the averaged correlation for the interannual anomalies between

374   ENSMEAN and the individual reanalyses is significant at a 99% confidence level in this region

375   (Fig. 3), i.e., the EOF-1 variability in this region is realized in most of the reanalyses at least in

376   terms of its sign. The ENSMEAN interannual MLD anomaly averaged over this region is very

377   coherent with the PC-1 (Fig. 6a) and also by and large vary with the interannual MLD anomalies

378   for the individual reanalyses as shown in Fig. 6b. These results support the idea that the rather

379   large ensemble spread seen in Fig. 2d is caused by the spread of the amplitude of the variation,

380   rather than on the sign of the MLD anomaly. It is also shown that the ensemble spread does not

381   change much during the whole 1948-2012 period. Therefore, the wintertime MLD variability in

382   this region generally maintains its correlation to the wintertime PDO index during the entire

383   period.

384

385   The above results introduce the variability on interannual time scales. Previous studies reported

386   the influence of the PDO on the decadal time scale. In our result, the MLD anomalies of

387   ENSMEAN averaged over the eastern part of the CMW formation region (green line in Fig. 6b)

388   is −17 m for the period before the regime shift associated with the PDO (1972-1976), which

389   increases to +18 m for the period after the regime shift (1977-81). This is in broad agreement to

390   previous observational and modelling studies focusing on the differences between the periods

391   before and after the 1976-1977 regime shift (e.g., Yasuda and Hanawa 1997; Ladd and Thompson

392   2002). Figure 6c shows the smoothed time series for the PC-1 and the wintertime PDO index via

393   a band-pass filter of 7-54 years based on the Fourier transform, which illustrates the presence of

394   a significant correlation between these time series on the decadal time scale (the correlation

395   coefficient is 0.74 for the 1955-2005 period), although the amplitude of the multi-decadal MLD

396   variability appears smaller than that of the multi-decadal PDO variability. Qu and Chen (2009)

397   investigated the MLD variability in relation to the variability of the annual subduction rate on the

398   decadal time scale in the North Pacific. They demonstrated that the time evolution of the

399   combined (MLD and subduction rate) variability correlates with the PDO index although they

400   also described that their results (especially for the first half of their simulation for 1950-2003)

401   could be influenced by both inaccurate forcing and inappropriate initial conditions of the model.

402   Our results using an ensemble of the reanalyses are in good agreement with these past studies.

403

404   **3.3 Variability in the eastern subtropical and subarctic regions**

405

406   The EOF-1 pattern (Fig. 5a) also shows interannual anomalies in the surrounding region with an

407   opposite sign to those in the western-central North Pacific. Three regions with relatively large

408   interannual anomalies are highlighted in this study: the ESTMW formation region (145°W-135°

409   W, 22°N-30°N, green square in Fig. 5a), the central Alaskan Gyre (160°W-140°W, 45°N-53°N,

410   orange square in Fig. 5a) and the Bering Sea (175°E-170°W, 53°N-60°N, red square in Fig. 5a).

411   The ensemble spread (Fig. 2d) averaged over each of these regions is 12 m, 7 m and 22 m,

412   respectively. The averaged correlations for the interannual anomalies between ENSMEAN and

413   the individual reanalyses are at a 95% confidence level in the ESTMW formation region and the

414   central Alaskan Gyre (Fig. 3). On the other hand, the correlation is low in the Bering Sea and

415   therefore not much data is used for the EOF analysis there (i.e., the data in the green-shaded area

416   in Fig. 3 are eliminated from the EOF analysis). Accordingly, we consider the MLD variability of

417   ENSMEAN in the Bering Sea to be not reliable, although the year of coldest wintertime SST,

418   1976 (2008) over the 1970-2008 period (after 2005), as reported in a previous study (Zhang et al.

419   2010) corresponds to the year of greatest wintertime MLD of ENSMEAN (not shown).

420

421   Figure 7 compares the PC-1 and the ENSMEAN interannual anomalies of the wintertime

422   maximum MLDs in the ESTMW formation region (Fig. 7a) and the central Alaskan Gyre (Fig.

423   7b). The MLD anomalies (green lines) in both regions generally show negative correlations with

424   the PC-1 (red lines) and thus with the wintertime PDO index (from Fig. 6) on both the interannual

425   and decadal time scales. The interannual MLD anomalies in the ESTMW formation region (Fig.

426   7a) are consistent with the previous study for the ESTMW variability during the 1991-2000 period

427   (Toyoda et al. 2011) but using an older version of the K7-ODA (ESTOC) reanalysis used in this

428   study (Table 1). In addition, the present results reveal that the ESTMW formation region is located

429   in the periphery of the PDO pattern with positive SST anomalies when the PDO index is positive.

430   This was not resolved in the SST patterns of the PDO as shown in previous studies (e.g., Mantua

431   et al. 1997) and thus has not been argued before.

432

433   Figure 7a exhibits that the negative correlation between the MLD anomalies and PC-1 on both

434   the interannual and decadal time scales generally holds during the entire time record. It is also

435   shown that the ensemble spread does not change much during the whole 1948-2012 period. These

436   facts support that ENSMEAN represents realistic features for both the interannual and decadal

437   variabilities in the ESTMW formation region. In contrast, over the central Alaskan Gyre (Fig. 7b)

438   the ensemble spread values are remarkably larger before 2000 than after 2001. This suggests that

439   in this region the data constraint during the assimilation is relatively weak without the Argo

440   observations. Note that the ensemble spread values become even smaller after 2004 possibly due

441   to the full deployment of the Argo array. The differences in phase between the smoothed time

442   series of the interannual MLD anomalies and PC-1, particularly before 1970, might reflect this

443   deficiency. Based on observations at Ocean Station Papa, Freeland and Cummins (2005)

444   demonstrated that the wintertime MLDs were shallower during El Niño events (1983, 1998 and

445   2003). Our result is qualitatively consistent with their findings. In addition, positive anomalies in

446   the late 1960s and early 1970s and negative anomalies from the middle of 1970s to the middle of

447   1980s are evident (Fig. 7b), similar to the observational reports (Fig. 10 of Freeland and Cummins

448   (2005); Fig. 4 of Li et al. (2005)). Moreover, Li et al. (2005) indicated that the annual maximum

449   MLDs appear in winter for the 1957-1976 period but in spring (April) for the 1977-1996 period

450   at several stations along the Line P (between the Station Papa and Vancouver Island) with

451   deepening of the spring ML taking place recently. In our result, the percentage of the April

452   occurrence of the annual maximum MLDs in the Alaskan Gyre increases, although the most

453   frequent month is still March (Fig. 7c). Such a change in the seasonal cycle of MLD should also

454   be important for the ecosystem and thus fisheries in this region. The physical mechanism remains

455   for future work.

456

3.4 Variability in the STMW formation region

458

459   The EOF-2 pattern is characterized by the prominent variability in the Kuroshio recirculation gyre

460   region (Fig. 5c), where the mean wintertime MLDs are large (Fig. 4a) associated with the STMW

461   formation. The ensemble spread of the interannual anomalies (Fig. 2d) averaged over this region

462   (140°E-160°E, 28°N-36°N, purple box in Fig. 5c) is 23 m and the averaged correlation for the

463   interannual anomalies between ENSMEAN and the individual reanalyses is significant at a 95%

464   confidence level (Fig. 3). As shown in Fig. 8a, the time series of the ENSMEAN MLD anomalies

465   averaged over this region and PC-2 show coherent evolution on both the interannual and decadal

466   time scales. In addition, the ensemble spread generally maintains similar values over the entire

467   period, although a consistent flattening is observed in the last decade. According to these results,

468   it can be considered that both the interannual and decadal variabilities in this region as reproduced

469   in ENSMEAN are generally robust and well captured by the EOF-2 during the whole 1948-2012

470   period.

471

472   Recent observational studies regarding the STMW and wintertime MLD variations in this region

473   have pointed out the interesting features: For example, shallower MLDs were seen in 1997-1999

474   from the analysis for 1993-2004 by Qiu and Chen (2006; their Fig. 4b). Sugimoto and Hanawa

475   (2010) showed that the STMWs were thinner in the late 1990s and thicker in the middle of 2000s

476   from data for 1993-2008. The MLD anomalies in ENSMEAN (Fig. 8a) are generally consistent

477   with these observational studies.

478

479   Comparison between the PC-2 and time series of the summertime core temperatures of the STMW

480   along the 137 °E line conducted by the JMA (Fig. 8b) provides another validation for the

481   interannual anomalies. It can be confirmed that, when the PC-2 is significantly negative (e.g., in

482   winter 1998), the STMW temperature is relatively high (e.g., in summer 1999) with the time lag

483   of about 1.5 year, since the EOF-2 is estimated from winter MLDs. The lagged (the EOF-2 leading

484   by 1.5 year) correlation coefficient for the PC-2 and the STMW core temperature for the 1981-

485   2011 period (after removal of the background trend) is −0.46, which is significant at a 99%

486   confidence level.

487

488   The above historical observations by the JMA include the geochemical parameters, which

489   provides a valuable source for the independent validation of our result. Figure 8c compares the

490   PC-2 and time series of nitrate concentration and AOU at the STMW density ($25.2\sigma_\theta$) between

491    $28°N$ to $32°N$ along the $137°E$ line. These geochemical parameters are relatively large (small)

492   when the PC-2 is negative (positive) with the time lag of a few years. It can be considered that

493   the lower values initiated at the STMW formation in the surface ML are better maintained in the

494   thermocline layer when the influence of the surrounding water is relatively small due to the

495   relatively thick STMW. The consistent relationship between the PC-2 and geochemical

496   parameters seen after the late 1960s supports a robust reproduction of the MLD variability

497   associated with the STMW variability in our result.

498

499

500   **3.5 Attribution of the variability in the STMW formation region**

501

502   Previous studies investigated the responses of the STMW (and wintertime MLDs in its formation

503   region) to the Aleutian Low activity with the time lag of a few years. Qiu et al. (2007) indicated

504   that the state of the Kuroshio Extension jet varies in response to the PDO forcing with the time

505   lag of about 4 years. The former strongly influences the STMW thickness (Qiu and Chen 2006).

506   For example, thicker STMW with greater wintertime MLDs is formed when the Kuroshio

507   Extension jet is stable. On the other hand, Sugimoto and Hanawa (2010) indicated the important

508   role of the WP forcing in determining the main thermocline depth in the Kuroshio recirculation

509   gyre region (with the time lag of about 3 years), which affects the STMW thickness.

510

511   In this study, we investigate the relationship between the PC-2, which represents the wintertime

512   MLD variability in the STMW formation region, and the PDO/WP time series. While the EOF-1

513   structure and its intensity are discussed using the wintertime PDO index (as in Ladd and

514   Thompson (2002) for example), seasonal changes of the indices might need to be taken into

515   consideration in terms of the delayed response, although the north-south dipole SLP anomalies of

516   the WP pattern are stronger in winter (Barnston and Livezey 1987). In fact, the wintertime WP

517   index was underlined to explain the Aleutian Low variability in Sugimoto and Hanawa (2009),

518   whereas the wind stress curl field regressed to the WP index in respective months was used in

519   Sugimoto and Hanawa (2010). As for the PDO index, the wintertime and annual time series are

520   equivalent with the correlation coefficient of 0.90 for the 1951-2012 period, which is much higher

521   than that for the WP index (0.42). Hence we use the annual PDO time series and both the annual

522   and wintertime WP time series in this subsection.

523

524   The lagged relationship of the above time series is shown in Fig. 9, in which positive MLD

525   anomalies represented by the positive PC-2 values in 2003 and 2004 (red line) are suggested be

526   generated by the dynamical response to the Aleutian Low activity around 1998-1999 (positive

527   values of the PDO (Fig. 9a), annual WP (Fig. 9b) and wintertime WP (Fig. 9c) indices), via the

528 westward propagation of baroclinic Rossby waves (e.g., Qiu et al. 2007; Sugimoto and Hanawa

529 2010). Figure 10a shows the correlation coefficients among these time series for each time lag.

530 Significant correlation at a 99% confidence level is only obtained by the simultaneous correlation

531 between the PC-2 and wintertime WP index. We will discuss this relation later. Although the

532 relation that the PDO index leads the PC-2 by 1 or 2 years is visible in 2000s (Fig. 9a), significant

533 correlation for such a time lag range (e.g., between −5 and −1 year) is not obtained from our long-

534 term analysis (Fig. 10a). Further, no significant correlation between the PC-2 and

535 annual/wintertime WP index is found for the time range of a few years by which the PC-2 lags or

536 leads the WP index.

537

538 The time series as shown in Fig. 9 rather emphasize the year-to-year variations. In general, the

539 dynamical response of the ocean to atmospheric disturbances takes place on longer time scales.

540 Therefore, we examine in the following the relationship between low-pass filtered time series

541 (Fig. 10b-d). No significant positive correlation for the PC-2 lagging the PDO or annual WP

542 indices is found (Fig. 10b, c, respectively). In contrast, the PC-2 and wintertime WP index low-

543 pass filtered by windows between 3-6 years exhibit significant positive correlation with the time

544 lags between 2-4 years (Fig. 10d). In particular, the correlation coefficient for the 3-year lag and

545 5-year low-pass filtered is significant at a 99% confidence level. This time lag is consistent with

546 the result of Sugimoto and Hanawa (2010). Note that the annual WP plot (Fig. 10c) also shows

547 positive values in the same range but these are much smaller and not significant. Therefore, the

548 wintertime WP index is plausible to explain the PC-2 with the time lag of 3 years (as the

549 wintertime WP index leads the PC-2) from our analysis.

550

551 Figure 10d also indicates significant positive correlations with the time lag of 3 years as the PC-

552 2 leads the wintertime WP index. Since a 3-year delayed response of the atmosphere is unlikely,

553 this can be attributed to the oscillatory feature of the wintertime WP index of about 6 years, which

554 is generally visible in Fig. 9c. In between these positive values, significant negative values are

555 visible with zero time lag, as seen in the plot of the raw time series (Fig. 10a) as described above.

556 From this result, we can consider that negative (positive) WP pattern is generated when the PC-2

557 is positive (negative). Therefore, the wintertime SST anomalies associated with the EOF-2 likely

558 act to force the atmosphere to generate the wintertime WP teleconnection pattern with the opposite

559 sign of the PC-2 (and the previous WP peak about 3 years before). This in turn changes the wind

560 stress field in the central North Pacific, which eventually influences the STMW formation region

561 as the sign of the PC-2 reverses with the time lag of about 3 years. This chain of processes leads

562 to the PC-2 cycle of about 6 years as discussed above (Fig. 10d).

563

564 Figure 11 shows the spectrum analysis for the PC-2 and the wintertime WP index. The power

565 spectra based on the maximum entropy method indicate a clear peak at the period of 5-10 years

566 for each of the time series. This is consistent with the aforementioned cycle of about 6 years.

567 However, it is known that the spectrum analysis based on the maximum entropy method

568 sometimes gives a false peak. In order to validate the above spectral peaks, another spectrum

569 analysis based on the fast Fourier transform is also conducted. Note that the distribution from this

570 analysis is generally rather noisy. For both time series, relatively large values are also obtained at

571 the period of 5-10 years when based on the fast Fourier transform. Although the resolution of

572 these analyses might not be enough to determine a 6-year cycle, these analyses at least support

573 the periodicities of both the PC-2 and the wintertime WP index around this period.

574

575 Figure 12 shows the regressed patterns to the PC-2 of the SLP, SST and surface turbulent heat

576 flux (THF; sum of latent and sensible heat fluxes; positive upward) fields. The regressed SLP

577 pattern (Fig. 12a) is almost the same as the negative wintertime WP pattern (e.g., Fig. 5 of

578 Sugimoto and Hanawa (2009)), which supports the large negative correlation between the PC-2

579 and wintertime WP index with zero time lag (Fig. 10d). Over most of the North Pacific, the SST

580 and THF anomalies have opposite signs (Fig. 12b). For example, the positive anomalies of THF

581 release to the atmosphere correspond to the negative SST anomalies in the south of Japan.

582 However, in the eastern part of the Kuroshio Extension region (yellow box approximately), there

583 exists a region where the anomalies have the same sign (positive) allowing the SST to increase

584 the THF and force the atmosphere. Note that this result is only slightly dependent on the forcing

585 dataset, differing little when the CORE dataset is used instead of the JRA-55 dataset as in Fig. 12.

586

587 Qiu and Chen (2006) indicated that the STMWs are relatively thick (thin) and thus the wintertime

588 MLDs in the STMW formation region are relatively large (small) when the Kuroshio Extension

589 jet is relatively strong and stable (weak and unstable). Several studies confirmed their point (see

590 Oka and Qiu 2012). Since the PC-2 represents the wintertime MLD variability in this region, the

591 above indication means that the Kuroshio Extension jet is relatively strong and stable (weak and

592 unstable) when the PC-2 is positive (negative). The state of the Kuroshio Extension jet possibly

593 affects the SSTs in the eastern part of the Kuroshio Extension: relatively higher (lower) SSTs can

594 be induced by the strong (weak) advection of the warm water, which leads to the positive

595 (negative) THF anomalies in this region, and thereby works on the atmosphere to generate the

596 negative (positive) WP teleconnection pattern. In fact, the core of the low pressure anomalies are

597 located around 180°, 35°N -40°N corresponding to a large positive SST anomaly region (Fig.

598 12b). Note that the PDO pattern also exhibits the large SST anomalies in this region although the

599 maxima of both SST and SLP are located to the east. Therefore difference in the SST distribution

600   between the EOF-1 (PDO index) and EOF-2 (wintertime WP index) might be important in forcing

601   the atmosphere. A full description of the process for the 6-year oscillation including the oceanic

602   EOF-2 and atmospheric WP patterns awaits future work.

603

604

605   **4 Conclusion**

606

607   We have performed an EOF analysis for the wintertime MLD anomalies in the North Pacific

608   derived from an ensemble of 17 global ocean reanalyses. To ensure the validity of the analysis,

609   we use only data in the region where the ensemble members consistently represent the MLD

610   variability, by taking account of the correlation between the individual reanalyses and ensemble

611   mean. The EOF-1 represents the MLD anomalies centered in the eastern part of the CMW

612   formation region in phase opposition with those in the ESTMW formation region and central

613   Alaskan Gyre and its PC highly correlates with the PDO index on both the interannual and

614   decadal time scales. The EOF-2 represents the MLD variability in the STMW formation region

615   and its PC correlates with the wintertime WP index with the time lag of about 3 years.

616

617   By using the global ocean reanalyses obtained through data assimilation approaches that

618   combine ocean models and observations, an integrated analysis of the important MLD features

619   in the whole North Pacific during the 1948-2012 period is provided in this study. In fact, the

620   MLD variabilities represented by the EOF modes are by and large consistent with previous

621   studies that mainly focused on their particular events or locations (e.g., the regime shift in 1976-

622   1977). In addition, the ensemble use of the reanalyses allows more quantitative discussion. The

623   robustness of the variabilities in the key regions for the water mass formation in the North

624   Pacific is generally confirmed by using information on the uncertainty of the ensemble mean,

625   which is measured by the ensemble spread of the reanalyses.

626

627   It is obvious that the historical observations are of fundament importance, without which neither

628   evaluation of the analysis nor realistic constraint to the assimilative models is possible. On the

629   other hand, the present study shows the great potential of the ensemble reanalyses for

630   investigating the climate variability. For example, mechanism of the recent deepening of the

631   spring ML in the Alaskan Gyre (Li et al. 2005) as reproduced in the reanalysis ensemble mean

632   can be investigated utilizing variables other than MLD. To carry this out, however, further

633   validation studies for the reanalysis products from various aspects as attempted in the ORA-IP

634   (e.g., Storto et al. 2015; see Balmaseda et al. 2015) are required.

635

636   To this date, conflicting causes have been suggested for the MLD variability in the STMW

637   formation region. This study provides the answer to the long-standing debate based on the long-

638   term assimilation products, that is, the meridional movement of the Aleutian Low is responsible

639   for the MLD variability in the STMW formation region. Furthermore, an oscillation of about 6

640   years which includes the WP teleconnection pattern in the atmosphere and the oceanic MLD

641   variability in the STMW formation region is first detected in this study. It is demonstrated that

642   the wintertime SST anomalies in the eastern part of the Kuroshio Extension associated with the

643   EOF-2 force the WP pattern with the opposite sign of the PC-2. This WP pattern induces the

644   change in the surface wind stress field in the central North Pacific, which, via the oceanic

645   dynamical response, eventually reverses the sign of the PC-2 with the time lag of about 3 years,

646   leading to about 6 years for the cycle of this process. The SST anomalies in the eastern part of

647   the Kuroshio Extension are possibly attributed to the variation in the Kuroshio Extension jet,

648   since the latter was pointed out by previous studies to have a close relation to the wintertime

649   MLD variability in the Kuroshio recirculation gyre region and hence the EOF-2. Although a full

650   description of the process remains for future work, identifying the oscillation of about 6 years in

651   this study might be able to give a new insight to understand the North Pacific climate variability,

652   such as in relation to the influence of the El Niño-Southern Oscillation of about 4 years and the

653   PDO of about 10 years.

654

655

656   **Acknowledgements**

657

668

669

670   **References**

671

672   Akima H (1970) A new method of interpolation and smooth curve fitting based on local

673   procedures. J Assoc Comput Mach 17:589-603

674

675   Balmaseda MA, Hernandez F, Storto A, Palmer MD, Alves O, Shi L, Smith GC, Toyoda T,

676   Valdivieso M, Barnier B, Behringer D, Boyer T, Chang YS, Chepurin GA, Ferry N, Forget G,

677   Fujii Y, Good S, Guinehut S, Haines K, Ishikawa Y, Keeley S, Köhl A, Lee T, Martin M, Masina

678   S, Masuda S, Meyssignac B, Mogensen K, Parent L, Peterson KA, Tang YM, Yin Y, Vernieres

679   G, Wang X, Waters J, Wedd R, Wang O, Xue Y, Chevallier M, Lemieux JF, Dupont F, Kuragano

680   T, Kamachi M, Awaji T, Caltabiano A, Wilmer-Becker K, Gaillard F (2015) The Ocean

681   Reanalyses Intercomparison Project (ORA-IP). J Operational Oceanogr 8:s80-s97.

682   doi:10.1080/1755876X.2015.1022329

683

684   Barnston AG, Livezey RE (1987) Classification, seasonality and persistence of low-frequency

685   atmospheric circulation patterns. Mon Wea Rev 115:1083-1126

686

687   de Boyer Montegut C, Madec G, Fischer AS, Lazar A, Iudicone D (2004) Mixed layer depth

688   over the global ocean: An examination of profile data and a profile-based climatology. J

689   Geophys Res 109:C12003. doi:10.1029/2004JC002378

690

691   Deser C, Alexander MA, Timlin MS (1996) Upper-ocean thermal variations in the North Pacific

692   during 1970-1991. J Clim 9:1840-1855

693

694   Freeland HJ, Cummins PF (2005) Argo: a new tool for environmental monitoring and

695   assessment of the world's oceans, an example from the NE Pacific. Prog Oceanogr 64:31-44.

696   doi:10.1016/j.pocean.2004.11.002

697

698   Hanawa K, Talley LD (2001) Mode waters. In: Sieldler G, Church J, J. Gould J (eds) Ocean

699   Circulation and Climate. Academic Press, NewYork, pp 373-386

700

701   Hautala SL, Roemmich DH (1998) Subtropical mode water northeast Pacific Basin. J Geophys

702   Res 103:13055-13066

703

704   Hosoda S, Ohira T, Sato K, Suga T (2010) Improved description of global mixed-865 layer

705   depth using Argo profiling floats. J Oceanogr 66:773-787. doi:10.1007/s10872-866 010-0063-3

706

707   Huang RX, Qiu B (1994) Three-dimensional structure of the wind-driven circulation in the

708   subtropical North Pacific. J Phys Oceanogr 24:1608-1622

709

710   Ishii M, Shouji A, Sugimoto S, Matsumoto T. (2005) Objective analyses of sea-surface

711   temperature and marine meteorological variables for the 20th century using ICOADS and the

712   Kobe Collection. Int J Climatol 25: 865-879

713

714   Joyce TM, Thomas LN, Bahr F (2009) Wintertime observations of subtropical mode water

715   formation within the Gulf Stream. Geophys Res Lett 36:L02607. doi:10.1029/2008GL035918

716

717   Kara AB, Rochford PA, Hurlburt HE (2003) Mixed layer depth variability over the global

718   ocean. J Geophys Res 108:3079. doi:10.1029/2000JC000736

719

720   Kawasaki T (1991) Long-term variability in the pelagic fish populations. In: Kawasaki T,

721   Tanaka S, Toba Y, Taniguchi A. (eds) Long-Term Variability of Pelagic Fish Populations and

722   Their Environment. Pergamon Press, New York, USA

723

724   Kobayashi S, Ota Y, Harada Y, Ebita A, Moriya M, Onoda H, Onogi K, Kamahori M,

725   Kobayashi C, Endo H, Miyaoka K, Takahashi K. (2015) The JRA-55 Renalysis: General

726   specifications and basic characteristics. J Meteor Soc Japan, in press. doi:20.2151/jmsj.2015-

727   0001.

728

729   Ladd C, Thompson LA (2002) Decadal Variability of North Pacific Central Mode Water. J Phys

730   Oceanogr 32:2870-2881

731

732   Large WG, Yeager SG (2004) Diurnal to decadal global forcing for ocean and sea-ice models:

733   the data sets and flux climatologies. Technical Note TN-460+STR, NCAR, Boulder, Colorado,

734   USA, 105 pp

735

736   Lee T, Awaji T, Balmaseda MA, Grenier E, Stammer D (2009) Ocean state estimation for

737   climate research. Oceanography 22:160-167. doi:10.5670/oceanog.2009.74

738

739   Levitus S (1982) Climatological atlas of the world ocean. NOAA/ERL GFDL, Princeton NJ

740   USA, 173 pp

741

742   Li M, Myers PG, Freeland H (2005) An examination of historical mixed layer depths along line

743   P in the Gulf of Alaska. Geophys Res Lett 32:L05613. doi:10.1029/2004GL021911

744

745   Mantua NJ, Hare SR, Zhang Y, Wallace JM, Francis RC (1997) A Pacific interdecadal climate

746   oscillation with impacts on salmon production. B Am Meteorol Soc 78:1069-1079

747

748   Masuzawa J (1969) Subtropical mode water. Deep Sea Res 16:463-472

749

750   Monterey G, Levitus S (1997) Seasonal Variability of Mixed Layer Depth for the World Ocean.

751   NOAA Atlas NESDIS 14. U.S. Government Printing Office, Washington DC USA

752

753   Newman M, Compo GP, Alexander MA (2003) ENSO-forced variability of the Pacific decadal

754   oscillation. J Climate 16:3853-3857

755

756   Oka E, Qiu B (2012) Progress of North Pacific mode water research in the past decade. J

757   Oceanogr 68:5-20. doi:10.1007/sl0872-011-0032-5

758

759   Oka E, Talley LD, Suga T (2007) Temporal variability of winter mixed layer in the mid-to high-

760   latitude North Pacific. J Ooceanogr 63:293-307.

761

762   Pedlosky J (1996) Ocean circulation theory. Springer Berlin Heidelberg, 456 pp.

763   doi:10.1007/987-3-662-03204-6

764

765   Peng G, Chassignet EP, Kwon YO, Riser SC (2006) Investigation of variability of the North

766   Atlantic Subtropical Mode Water using profiling float data and numerical model output. Ocean

767   Model, 13:65-85. doi:10.1016/j.ocemod.2005.07.001

768

769   Press WG, Teukolsky SA, Vetterling WT, Flannery BP (1992) Numerical Recipes in

770   FORTRAN: The Art of Scientific Computing Second Edition. Cambridge Univ Press,

771   Cambridge UK, 963 pp.

772

773   Qiu B, Chen S (2006) Decadal variability in the formation of the North Pacific Subtropical

774   Mode Water: Oceanic versus atmospheric control. J Phys Oceanogr 36:1365-1380

775

776   Qiu B, Chen S, Hacker P (2007) Effect of mesoscale eddies on subtropical mode water

777   variability from the Kuroshio Extension System Study (KESS). J Phys Oceanogr 37:982-1000.

778   doi:10.1175/JPO03097.1

779

780   Qu T, Chen J (2009) A North Pacific decadal variability in subduction rate. Geophys Res

781   Lett 36:L22602. doi:10.1029/2009GL040914

782

783   Schneider N, Miller AJ, Alexander MA, Deser C (1999) Subduction of decadal North Pacific

784   temperature anomalies: Observations and dynamics. J Phys Oceanogr 29:1056-1070

785

786   Senjyu T, Sudo H (1994) The upper portion of the Japan Sea proper water, its source and

787   circulation as deduced from isopycnal analysis. J Oceanogr 50:663–690

788

789   Speer K, Forget G (2013) Global distribution and formation of mode waters. In: Siedler G,

790   Griffies SM, Gould J, Church JA (eds) Ocean Circulation and Climate: A 21st Century

791   Perspective. Academic Press, New York, pp 211-226. doi:10.1016/B978-0-12-391851-2.00009-

792 X

793

794 Storto A, Masina S, Balmaseda M, Guinehut S, Xue Y, Szekely T, Fukumori I, Forget G, Chang

795 Y-S, Good SA, Köhl A, Vernieres G, Ferry N, Peterson KA, Behringer D, Ishii M, Masuda S,

796 Fujii Y, Toyoda T, Yin Y, Valdivieso M, Barnier B, Boyer T, Lee T, Gourrion J, Wang O,

797 Heimback P, Rosati A, Kovach R, Hernandez F, Martin MJ, Kamachi M, Kuragano T,

798 Mogensen K, Alves O, Haines K, Wang X (2015) Steric sea level variability (1993-2010) in an

799 ensemble of ocean reanalyses and objective analyses. Clim Dyn (in press). doi:10.1007/s00382-

800 015-2554-9

801

802 Suga T, Takei Y, Hanawa K (1997) Thermostad distribution in the North Pacific subtropical

803 gyre: The central mode water and the subtropical mode water. J Phys Oceanogr 27:140-152

804

805 Sugimoto S, Hanawa K (2009) Decadal and interdecadal variations of the Aleutian Low activity

806 and their relation to upper oceanic variations over the North Pacific. J Meteor Soc Japan 87:601-

807 619. doi:10.2151/jmsj.87.601

808

809 Sugimoto S, Hanawa K (2010) Impact of Aleutian Low activity on the STMW formation in the

810 Kuroshio recirculation gyre region. Geophys Res Lett 37:L03606. doi:10.1029/2009GL041795

811

812 Takahashi T, Feely RA, Weiss RF, Wanninkhof RH, Chipman DW, Sutherland SC, Takahashi

813 TT (1997) Global air-sea flux of CO_2: An estimate based on measurements of sea–air pCO_2

814 difference. P Natl Acad Sci, 94:8292-8299

815

816   Toyoda T, Awaji T, Masuda S, Sugiura N, Igarashi H, Mochizuki T, Ishikawa Y (2011)

817   Interannual variability of North Pacific eastern subtropical mode water formation in the 1990s

818   derived from a 4-dimensional variational ocean data assimilation experiment. Dynam Atmos

819   Oceans 51:1-25. doi:10.1016/j.dynatmoce.2010.09.001

820

821   Toyoda T, Fujii Y, Kuragano T, Kamachi M, Ishikawa Y, Masuda S, Sato K, Awaji T,

822   Hernandez F, Ferry N, Guinehut S, Martin M, Peterson KA, Good S, Valdivieso M, Haines K,

823   Storto A, Masina S, Köhl A, Zuo H, Balmaseda M, Yin Y, Shi L, Alves O, Smith G, Chang YS,

824   Vernieres G, Wang X, Forget G, Heimbach P, Wang O, Fukumori I, Lee T (2015)

825   Intercomparison and validation of the mixed layer depth fields of global ocean syntheses. Clim

826   Dyn (in press). doi:10.1007/s00382-015-2637-7

827

828   Trenberth KE, Hurrell JW (1994) Decadal atmosphere-ocean variations in the Pacific. Clim Dyn

829   9:303-319

830

831   Wallace JM, Gutzler DS (1981) Teleconnections in the geopotential height field during the

832   Northern Hemispheric winter. Mon Wea Rev 109:784-812

833

834   Yasuda T, Hanawa K (1997) Decadal changes in the mode waters in the midlatitude North

835   Pacific. J Phys Oceanogr 27:858-870

836

837   Yasuda I, Tozuka T, Noto M, Kouketsu S (2000) Heat balance and regime shifts of the mixed

838   layer in the Kuroshio Extension. Prog Oceanogr 47:257-278. doi:10.1016/S0079-

839   6611(00)00038-0

840

841 Wen C, Kumar A, Xue Y (2014) Factors contributing to uncertainty in Pacific Decadal Oscillation

842 index. Geophys Res Lett 41:7980-7986. doi:10.1002/2014GL061992

843

844 Xue Y, Balmaseda MA, Boyer T, Ferry N, Good S, Ishikawa I, Kumar A, Rienecker M, Rosati

845 AJ, Yin Y (2012) A comparative analysis of upper-ocean heat content variability from an

846 ensemble of operational ocean reanalyses. J Clim 25:6905-6929. doi:10.1175/JCLI-D-11-

847 00542.1

848

849 Zhang J, Woodgate R, Moritz R (2010) Sea ice response to atmospheric and oceanic forcing in

850 the Bering Sea. J Phys Oceanogr 40:1729-1747. doi:10.1175/2010JPO4323.1

851

852

853 **Tables**

854

855 **Table 1** Producing centers, contact parsons and duration of the syntheses used in this study

Synthesis	Center	Contact parson	Duration
(Observation-only analysis)			
EN3v2a	Met Office	S. Good	1993-2011
ARMOR3D	CLS	S. Guinehut	1993-2010
(Reanalysis)			
G2V3	Mercator Océan	F. Hernandez	1993-2011
C-GLORS	CMCC	A. Storto	1991-2011
UR025.4	U-Reading	M. Valdivieso	1993-2010
GloSea5	Met Office	M. Martin	1993-Jul. 2012
ORAS4	ECMWF	M. Balmaseda	1958-2011
ORAP5	ECMWF	H. Zuo	1993-2012
GECCO2	U-Hamburg	A. Köhl	1948-Nov. 2011

MERRA	GSFC/NASA/GMAO	G. Vernieres	1993-2011
ECCO-NRT	JPL/NASA	O. Wang	1993-2011
ECCO-v4	JPL/MIT/AER	X. Wang	1992-2010
ECDA	GFDL/NOAA	Y.-S. Chang	2005-2011
PEODAS	BoM	O. Alves	1980-2012
K7-ODA (ESTOC)	RCGC/JAMSTEC	S. Masuda	1975-2011
K7-CDA	CEIST/JAMSTEC	Y. Ishikawa	2000-2006
MOVE-G2	MRI/JMA	T. Toyoda	1993-2012
MOVE-CORE	MRI/JMA	Y. Fujii	1948-2007
MOVE-C	MRI/JMA	Y. Fujii	1950-2011

856   Durations submitted to the ORA-IP are sometimes shorter than those of the original syntheses

857

858

859   **Figures**

860

861
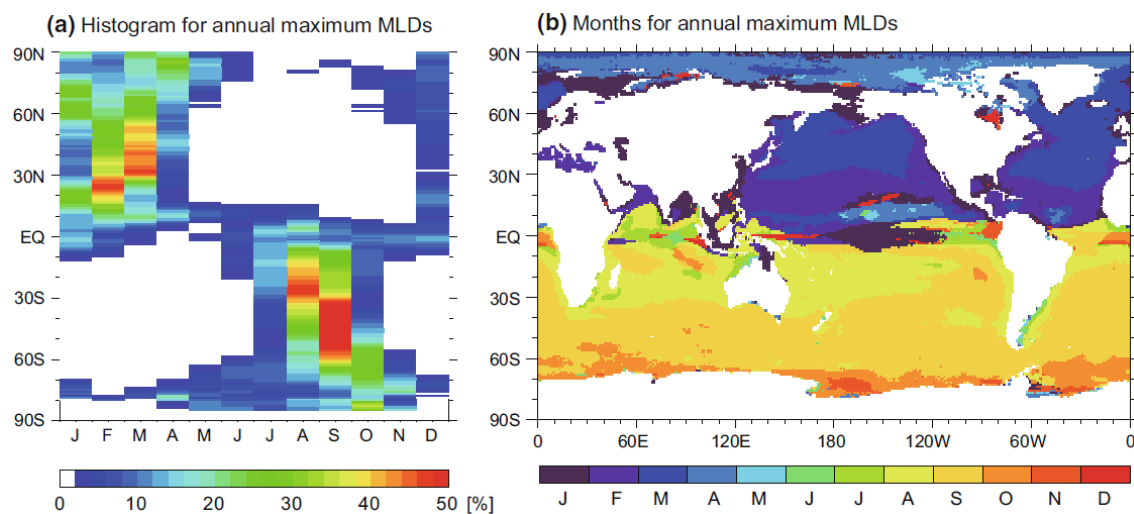
862   **Fig. 1** (a) Histogram for the occurrence of the annual maximum MLDs for each month and latitude

863   normalized by the zonal sum of the values (units in %). (b) Distribution of the months when the

864   annual maximum MLDs occur most frequently. The month of the annual maximum MLD

865   estimated for each grid point, year and synthesis is used for these plots.

866
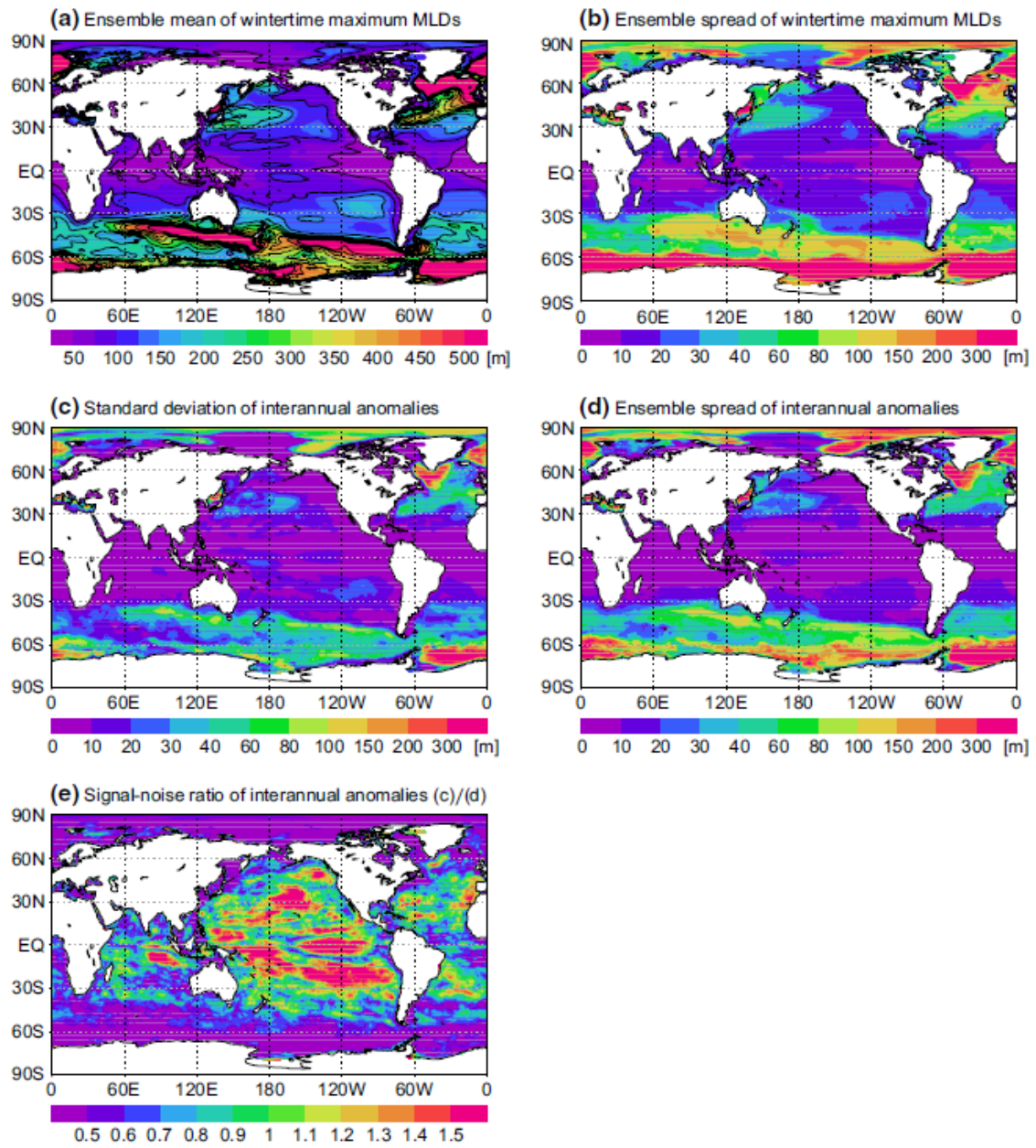
Fig. 2 Distributions of the ensemble mean (a) and spread (b) of the wintertime maximum MLDs, the standard deviation of the interannual anomalies of the ensemble mean wintertime maximum MLDs (c), the ensemble spread of interannual anomalies of the wintertime maximum MLDs (d) and signal to noise ratio of the interannual anomalies (e; defined here as (c) divided by (d)). Values are estimated from all the 17 reanalyses and averaged over the 2001-2011 period.
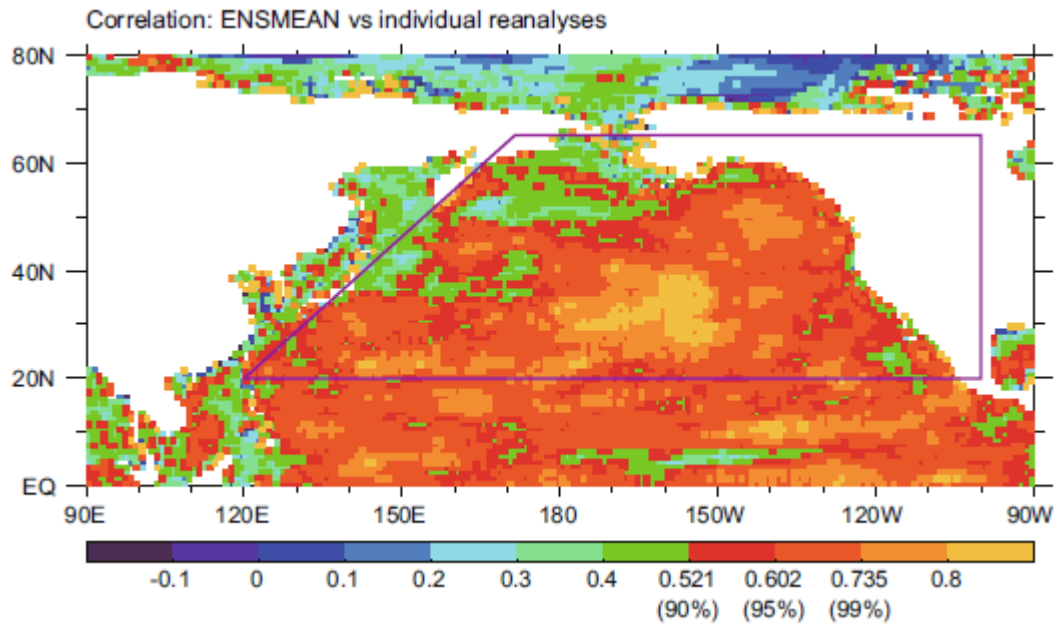
874

Fig. 3 Distribution of the averaged correlation coefficients of the wintertime maximum MLDs

between ENSMEAN and the individual 17 reanalyses for the 2001-2011 period. Note that the

color bar differs from that in Fig. 4. Values at the confidence levels of 90, 95 and 99% are

highlighted in this figure. Here, the sample size is the number of years, 11. The purple line

indicates the open ocean region of the North Pacific within which we use the data for the EOF

analysis (see text).

881
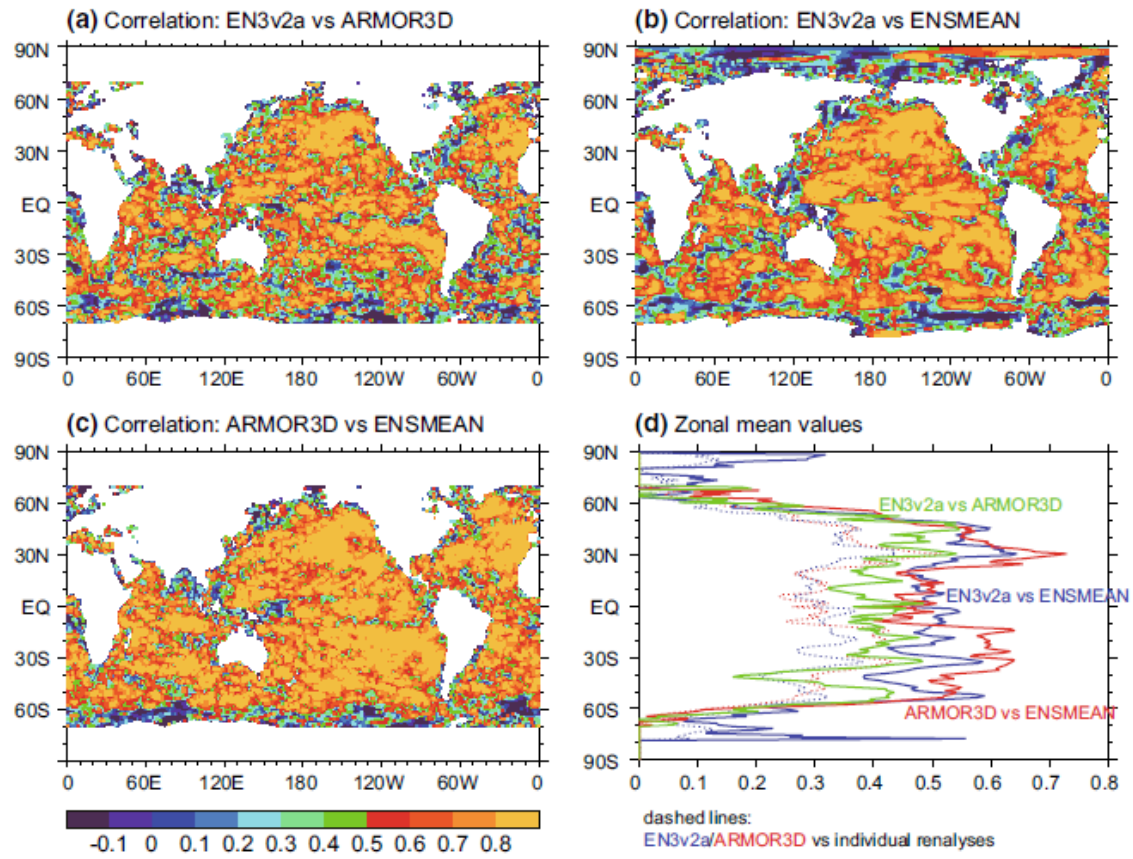
Fig. 4 (a-c) Distributions of correlation coefficients of the wintertime maximum MLDs between EN3v2a and ARMOR3D (a), between EN3v2a and ENSMEAN (b) and between ARMOR3D and ENSMEAN (c). Note that the color bar differs from that in Fig. 3. (d) Zonal mean values for the above distributions (a-c; solid lines) and the averaged correlation coefficients between EN3v2a/ARMOR3D and the individual 17 reanalyses (dashed lines). Winter maximum MLDs for the 2001-2011 period are used.
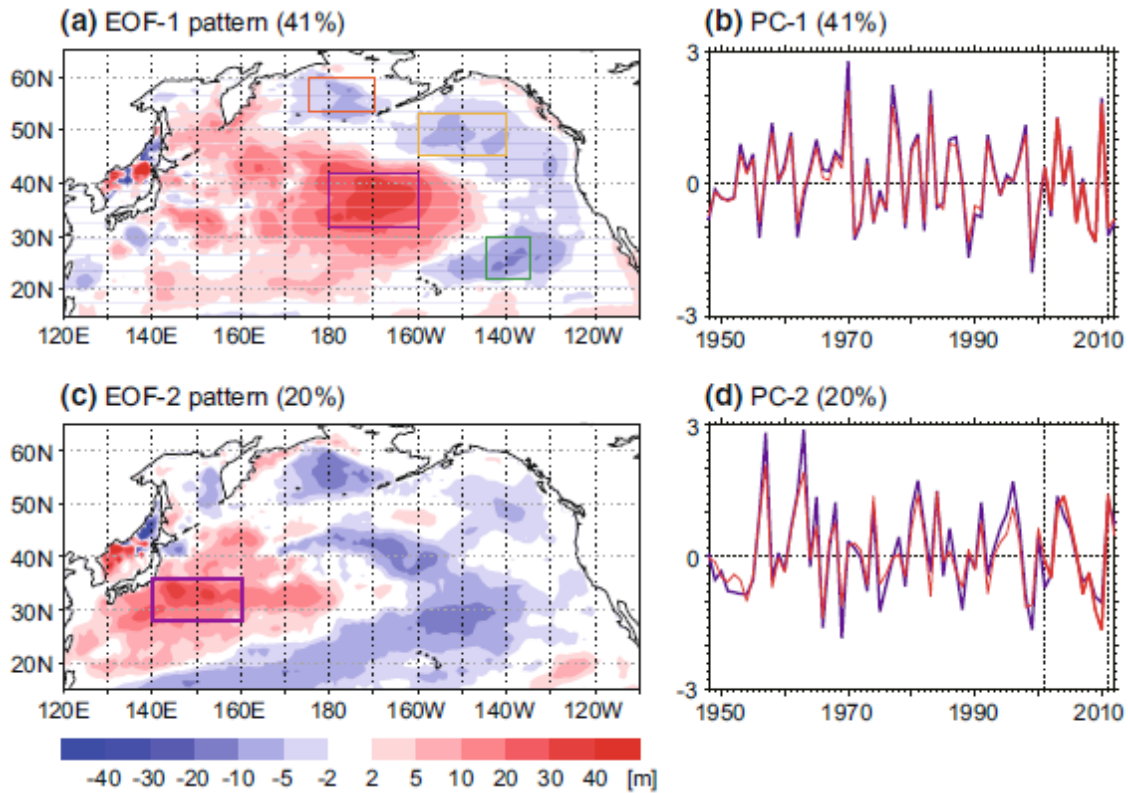
Fig. 5 (a) Pattern of the EOF-1 for the 2001-2011 period calculated from ensemble mean wintertime maximum MLDs. Boxes indicate the eastern part of the CMW formation region (purple), the ESTMW formation region (green), the central Alaskan Gyre (orange) and the Bering Sea (red). (b) PC-1 for the EOF analyses of the 2001-2011 (red) and 1948-2012 (blue) periods. (c, d) Same as (a, b) but for EOF-2 and PC-2. The purple box in (c) indicates the STMW formation region. Note that the EOF projection have been used both to fill spatial gaps and to extend the time series. Thus, projection values of the PCs are plotted in the region where data are rejected for the EOF analysis (e.g., in the Okhotsk Sea). Similarly, PCs for 2001-2011 are extended forward and back to the full 1948-2012 period by projection of the EOF patterns onto the ENSMEAN interannual anomaly field (thin red line).

(a) PC-1 and PDO time series

(b) MLD anomalies in the CMW region

(c) PC-1 and PDO time series (smoothed)

902
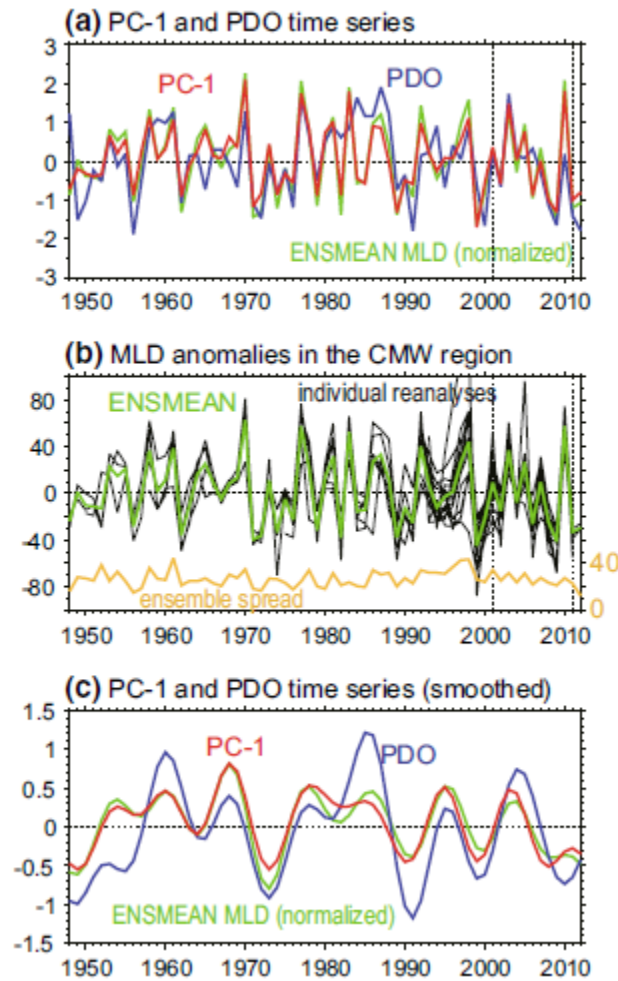
Fig. 6 (a) PC-1 (red) and the wintertime PDO time series (blue). For the PC-1, projected values

of the EOF-1 pattern are also plotted for the other period of the EOF analysis (2001-2011). Green

line denotes the interannual MLD anomalies of ENSMEAN averaged over the eastern part of the

CMW formation region (180°-160°W, 32°N-42°N; purple box of Fig. 5a; left axis) and

normalized by their standard deviation. (b) Time series of the interannual MLD anomalies

averaged over the eastern part of the CMW formation region (left axis) for the individual

reanalyses (17 black lines) and ENSMEAN (green line). In addition, time series of the ensemble

spread averaged over the same region are plotted (yellow line; right axis). Units are in meter. (c)

Same as (a) but smoothed by a band-pass filter for the 7-54 year band. Note that the lower

frequencies are cut in order to eliminate the trends of the time series.
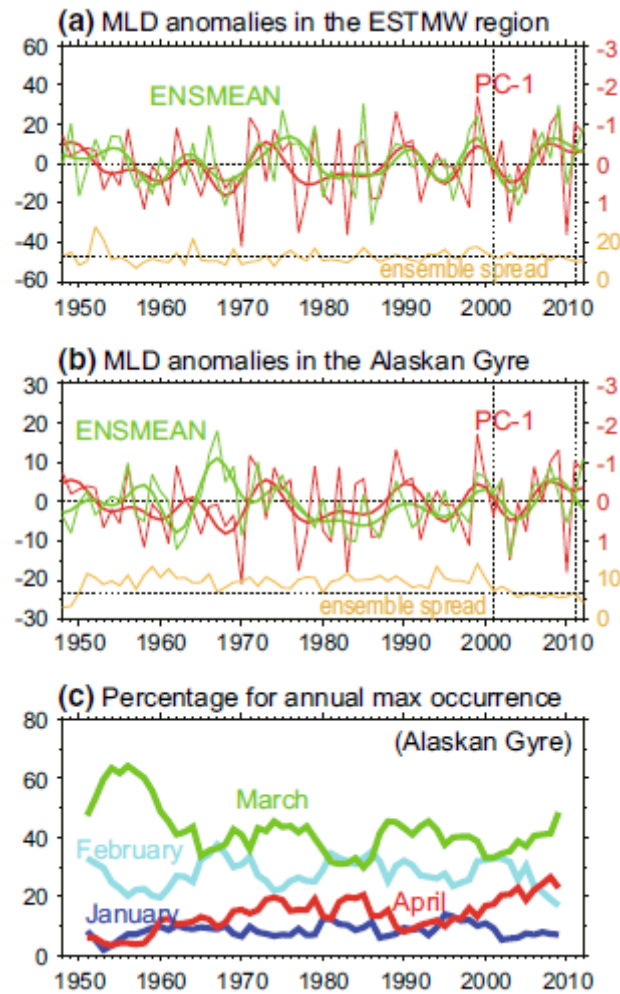
913

914

915 **Fig. 7** Raw (thin) and 7-year low-pass filtered (thick) time series of the interannual anomalies of

916 the wintertime maximum MLDs averaged over the ESTMW formation region (145°W-135°W,

917 22°N-30°N; green box of Fig. 5a; left axis) for ENSMEAN (green) and PC-1 (red; right axis in

918 red with the numbers upside down). Time series of the ensemble spread averaged over this region

919 (yellow; right axis in yellow). (b) Same as (a) but for the central Alaskan Gyre (160°W-140°W,

920 45°N-53°N; orange box of Fig. 5a). (c) Time series of percentages of each month for the

921 occurrence of the annual maximum MLDs in the central Alaskan Gyre. All the 17 reanalyses are

922 used.

923

924
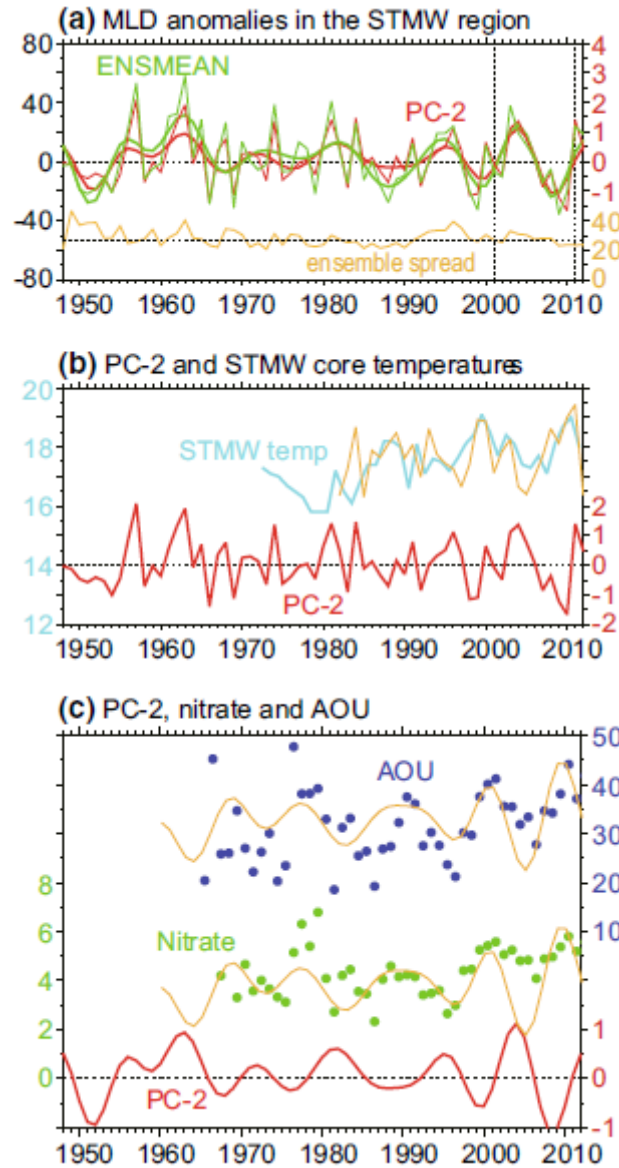
Fig. 8 (a) Same as Fig. 7 but for the STMW formation region (140°E-160°E, 28°N-36°N; purple

box of Fig. 5c) and PC-2. (b) PC-2 (red; right axis) and summertime temperatures in the STMW

core at 137°E (light blue; left axis). (c) PC-2 (red; right axis in red) and the annual mean values

of nitrate concentrations (green; left axis; units in μmol/kg) and AOUs (blue; right axis in blue;

units in μmol/kg) on the 25.2σθ surface between 28°N and 32°N along the 137°E line. The

summertime temperatures and annual mean nitrate concentrations and AOUs are plotted with a

forward offset of half a year. Yellow lines in (c, d) denote the unfiltered/filtered PC-2 but inverted

932   and lagged by 1.5 year.

933

934
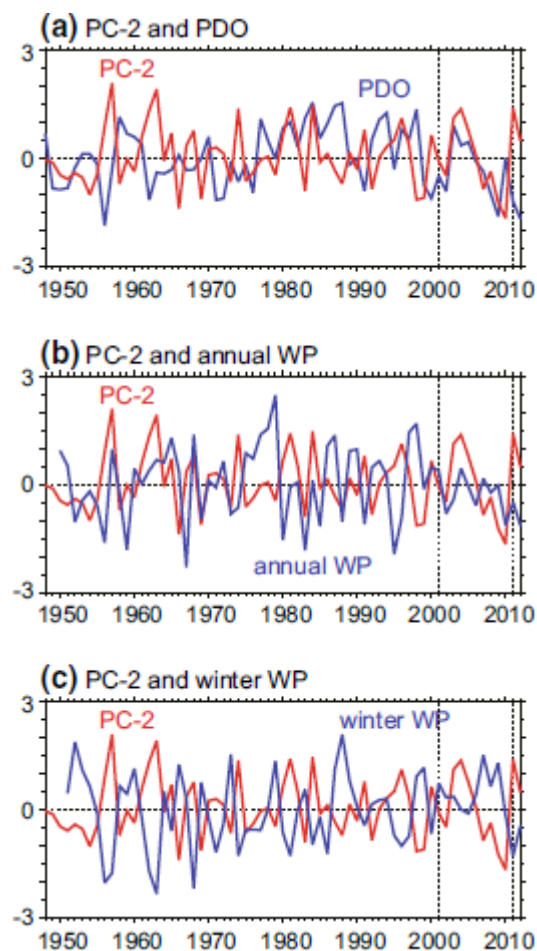
Fig. 9 Comparison of the PC-2 (red) with the time series of the annual PDO (a), annual WP (b)
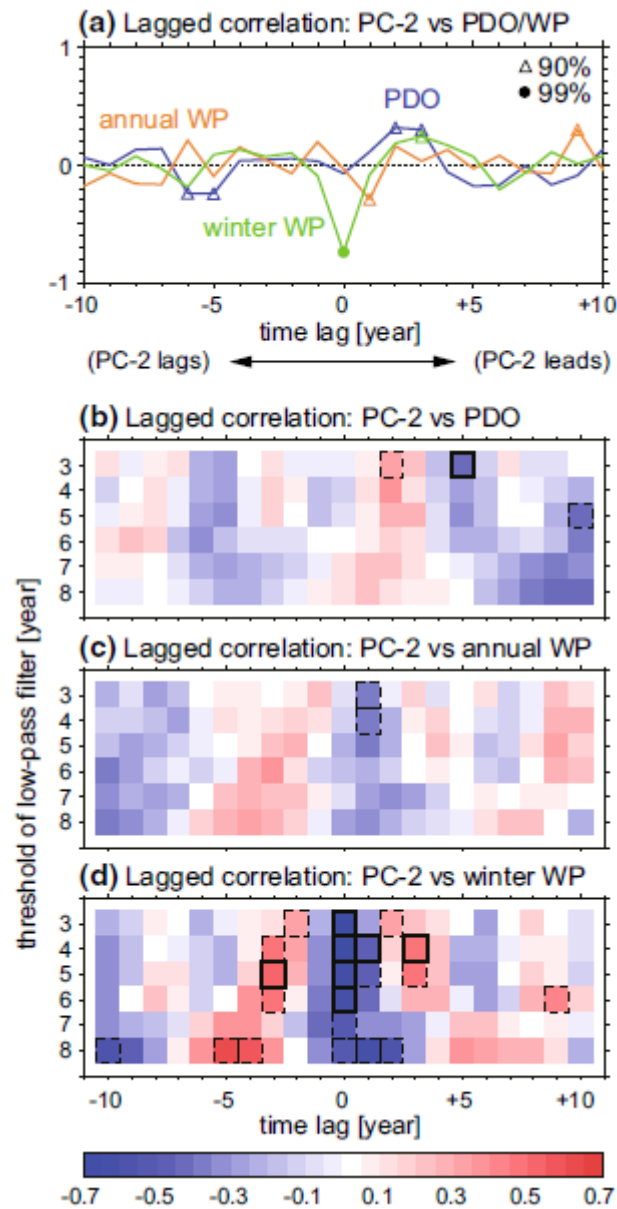
936   and wintertime WP (c) indices (blue).

937

Fig. 10 (a) Lagged correlation of the PC-2 with the time series of the PDO (blue), annual WP (yellow) and wintertime WP (green) indices. Positive (negative) lags indicate the lead (delay) of the PC-2 over the PDO/WP index. Triangle (circle) indicates the value at a 90% (99%) confidence level. (b) Lagged correlation between the low-pass filtered time series between the PC-2 and PDO index depending on the time lag (x-axis) and the number of years of the low-pass filter (y-axis). Dashed (solid) box indicates the value at a 90% (99%) confidence level. Note that the degree of freedom changes due to both the decrease in the analyzed period when considering a time lag,

946   and to the filtering of the high frequent variations. (c, d) Same as (b) but for the annual and

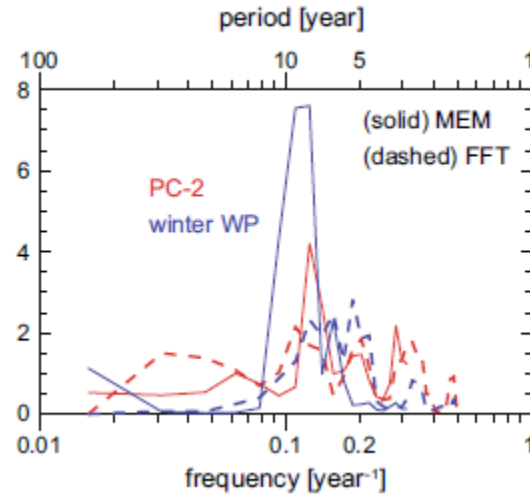947   wintertime WP indices, respectively.

948

949

950   **Fig. 11** Power spectra for the PC-2 (red) and the wintertime WP index (blue) for the 1948-2012

951   period. Solid lines are based on the maximum entropy method (with the number of poles of the

952   approximation of 20; see Press et al. 1992). Dashed lines are based on the fast Fourier transform

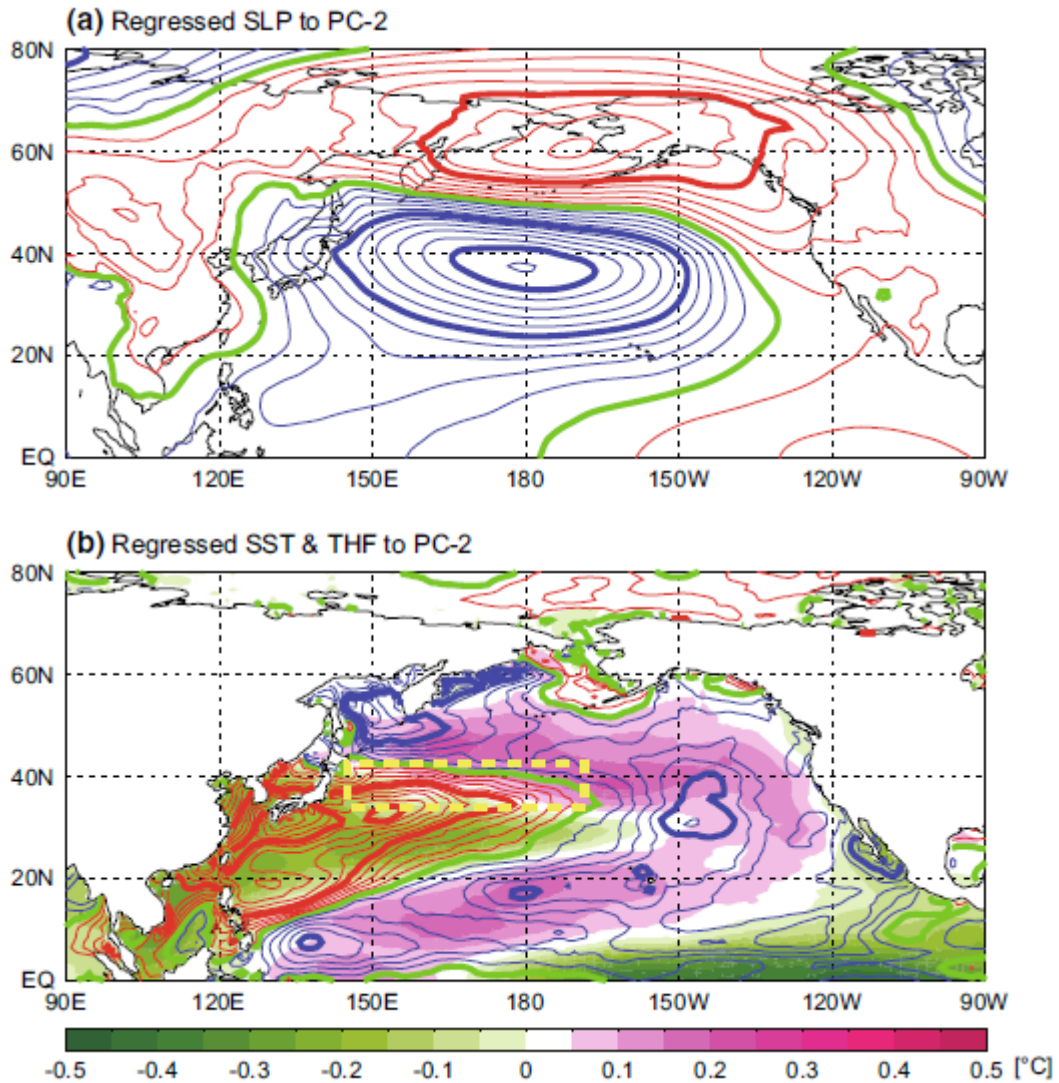953   method. 3-point running mean are taken for the latter.

954

Fig. 12 (a) Regressed SLP pattern to the PC-2. Contour intervals are 0.2 hPa. (b) Regressed SST (shade) and THF (contour; 2 W/m^2 intervals) patterns to the PC-2. The JRA-55 and COBE-SST dataset are used. Blue (red) lines denote contours of negative (positive) values. Zero contours are indicated by green lines. Yellow box in (b) indicate the Kuroshio Extension region approximately.